Supplementary Information

Copper-carbon dot aerogel: a high-performance mimetic peroxidase and its application for versatile colorimetric bioassays

Tao Zhang, Qianfen Zhuang and Yong Wang*

School of Chemistry and Chemical Engineering, Nanchang University, Nanchang 330031, China

* Corresponding author. Tel.: +86 791 83969500; fax: +86 791 83969500.

E-mail address: wangyong@ncu.edu.cn

Table of Contents

1. Experimental section

Reagents and chemicals. Adenine, sodium citrate trihydrate, 3,3',5,5'-tetramethylbenzidine (TMB), glucose oxidase (GOx), bovine serum albumin (BSA), and tris (hydroxymethyl) aminomethane (Tris) were bought from Sangon Biotech Co., Ltd. (Shanghai, China). Glucose (Glu), fructose, and sucrose were purchased from Sigma-Aldrich Co. (USA). Lactose was purchased from Lanji Technology Development Co., Ltd. (Shanghai, China). Acetic acid, copper nitrate trihydrate, hydrochloride acid and hydrogen peroxide (H_2O_2) were purchased from Sinopharm Chemical Reagent Co., Ltd. (Shanghai, China). Neocuproine, 4-nitrophenyl-α-D-glucopyranoside (NPGlu), acarbose hydrate, quercetin, oleanolic acid, terephthalic acid (TA), phenylalanine (Phe), glycine (Gly), cysteine (Cys), and uric acid (UA) was purchased from Aladdin Biochemical Technology Co., Ltd. (Shanghai, China). Acetylcholinesterase (AChE), α-glucosidase (α-Glu), alkaline phosphatase (ALP), cytochrome C (Cyt C), voglibose, gallic acid, and maltose were purchased from Yuanye Biotechnology Co., Ltd. (Shanghai, China). Lysozyme and trypsin were purchased from Solarbio Science & Technology Co., Ltd. (Beijing, China). Anhydrous sodium acetate purchased from Shanghai Macklin Biochemical Technology Co., Ltd. (Shanghai, China). All reagents were analytically pure, and deionized water was used in the whole experiment.

Apparatus. UV-Vis spectral and kinetic experiments were carried out with an Agilent-8453 ultraviolet spectrophotometer (Agilent Technologies, USA). Photoluminescence spectra (PL) were detected with an F-4600 fluorescence spectrophotometer (Hitachi, Japan). Scanning electron microscope (SEM) images coupled with elemental mapping were obtained by using a JSM-6701F microscope (JEOL Co., Japan). Transmission electron microscope (TEM) images were obtained by using a JEM-2100 microscope (JEOL Co., Japan) under an accelerating voltage condition of 200 kV. X-ray photoelectron spectroscopy (XPS) was taken on a Thermo Scientific KAlpha X-ray spectrometer (ThermoFisher, USA). Fourier transform infrared spectroscopy (FT-IR) was measured on a Bruker Alpha spectrometer (Bruker, Germany). Thermogravimetric analysis (TGA) was carried out under an N_2 atmosphere by using TGA 4000 thermogravimetric analyzer (PerkinElmer Co., USA) with a ramp rate of 10 °C/min. N_2 adsorption–desorption isotherms were measured at 77.3 K with a Quantachrome Autosorb IQ (Quantachrome Co., USA). The multi-point Brunauer–Emmett–Teller (BET) method was used to calculate the specific surface areas. The pore size distribution was evaluated using the quenched solid density functional theory (QSDFT) equilibrium model. The amount of the copper in the aerogels was measured using an Avio 200 inductively coupled plasma optical emission spectrometer (ICP-OES, PerkinElmer Co., USA). Electron paramagnetic resonance (EPR) measurements were done on a EMXplus model

spectrometer (Bruker, Germany), and 5,5-dimethyl-1-pyrroline-N-oxide (DMPO) was used as a radical spin-trapping agent.

Synthesis of CD_A. CD_A were hydrothermally synthesized using sodium citrate and adenine as the precursors. In brief, 0.101 g of adenine and 0.109 g of sodium citrate were dissolved in 20 mL of water. After ultrasonication for 5 min, the mixture was transferred into a 50 mL Teflon-lined stainless steel autoclave and reacted at 200 °C for 4 h. After cooling to room temperature, the supernatant was collected by centrifugation at 12,000 rpm for 10 min. After that, the resulting solution was dialyzed against water for 6 hours using a dialysis bag with a MWCO of 200 Da. Finally, the as-prepared solution was freeze-dried at −60 °C to obtain the dry CD_A product.

Synthesis of Cu-CD_A aerogels. Copper nitrate solution (500 μL, 1 M) was added into CD_A solution (10 mL, 1 mg/mL), and then mixed homogeneously. After the mixture remained stationary at room temperature for 30 s, bluish-green jellylike Cu-CD_A hydrogels were generated. Such the hydrogels were centrifuged at 12,000 rpm for 10 min, and then washed three times with water. By simple lyophilization, Cu-CD_A aerogels were prepared from the hydrogels.

Mimetic peroxidase activity of Cu-CD_A aerogels. The mimetic peroxidase activity of the Cu-CD_A aerogels was examined by a typical chromogenic reaction using 3,3',5,5' -tetramethylbenzidine (TMB) as a substrate. In brief, 200 μL of Cu-CD_A aerogels (1 mg/mL), 100 μL of TMB (10 mM), 600 μL of ultrapure water, and 1 mL of acetate buffer (200 mM, pH 4.0) were successively added and mixed thoroughly. Then, 100 μL of H_2O_2 (100 mM) was added into the mixture. After incubation for 5 min, the absorption spectra ranging from 500−800 nm were recorded with a UV-Vis spectrophotometer. A typical absorption peak of the blue oxidized TMB (oxTMB) can be observed at 652 nm. As a comparison, the reaction systems, *i.e.*, Cu-CD_A, Cu-CD_A+H_2O_2, Cu-CD_A+TMB, H_2O_2+TMB, and Cu-CD_A+H_2O_2+TMB, were also studied under the same conditions. The optimal conditions of Cu-CD_A amount, reaction time, buffer pH, and temperature for the catalytic oxidation of TMB based on Cu-CD_A aerogels were studied in detail.

Steady-state kinetic studies. Kinetic measurements of mimetic peroxidase property were performed by monitoring the time-dependent evolution of the absorbance at 652 nm of oxTMB using a UV-Vis spectrophotometer. The steady-state kinetic parameters of the substrate TMB or H_2O_2 were respectively estimated by changing the TMB concentration (0−2.0 mM) at the constant H_2O_2 concentration (5 mM) or changing the H_2O_2 concentration (0−40 mM) at the fixed TMB concentration (0.5 mM). The recorded data were fitted and analyzed by the following Michaelis-Menten equation:

$$v = v_{max} \times [S]/(K_m + [S]) \quad (1)$$

where v, v_{max}, K_m, and [S] refer to the initial chromogenic reaction rate, the maximum initial chromogenic reaction rate, the Michaelis−Menten constant, and the substrate concentration, respectively. The initial reaction rates of different substrate concentrations can be calculated on the basis of $v = (\Delta A/\Delta t) \times 1/\varepsilon b$ ($\varepsilon = 3.9 \times 10^4\ M^{-1}\cdot cm^{-1}$, $b = 1$ cm). The Michaelis−Menten constant K_m and the maximum initial reaction rate v_{max} can be usually estimated according to the double-reciprocal Lineweaver−Burk plot ($1/v = K_m/v_{max} \times 1/[S] + 1/v_{max}$).

Colorimetric bioassay of hydrogen peroxide. 200 μL of Cu-CD_A aerogels (1 mg/mL), 100 μL of TMB (10 mM) and 1 mL of acetate buffer solution (200 mM, pH 4.0) were sequentially added into a 5 mL plastic vial, and mixed well. Then, different concentrations of H_2O_2 were added into the mixture, and diluted with water to give a total volume of 2 mL. After incubation at 50 °C for 5 min, UV-Vis spectra of the resultant solution were recorded.

Colorimetric bioassay of glucose. 100 μL of GOx (1 mg/mL) and appropriate amounts of glucose solution were added into a 1.5 mL plastic vial, followed by the addition of 100 μL of Tris-HCl buffer (10 mM, pH 7.4) and dilution to 400 μL with water. After the mixture was incubated at 37 °C for 40 min, 200 μL Cu-CD_A aerogels (1 mg/mL), 100 μL TMB (10 mM), 1 mL of acetate buffer solution (200 mM, pH 4.0), and 300 μL water were sequentially added to give a total volume of 2 mL. Finally, UV-visible absorption spectra of the resultant solution were collected after incubation at 50 °C for 5 min.

Colorimetric bioassay of α-glucosidase. 100 μL of α-Glu with different activities, 200 μL 4-nitrophenyl-α-D-glucopyranoside (NPGlu, 200mM), and 50 μL GOx (1 mg/mL), were added into a 1.5 mL plastic vial, followed by the addition of 100 μL of Tris-HCl buffer (10 mM, pH 7.4). After the mixture was incubated at 37 ° C for 40 min, 200 μL Cu-CD_A aerogels (1 mg/mL), 100 μL TMB (10 mM), 1 mL of acetate buffer solution (200 mM, pH 4.0), and 250 μL water were sequentially added to give a total volume of 2 mL. Finally, UV-visible absorption spectra of the resultant solution were collected after incubation at 50 °C for 5 min.

Screening of α-glucosidase inhibitors and voglibose assay. 100 μL of AGIs, such as voglibose (0.5 mM), acarbose (5 mM), oleanolic acid (5 mM), gallic acid (5 mM), or quercetin (5 mM), were added into the α-Glu solution, and mixed well. After incubation at room temperature for 15 min, the resultant solution was analyzed by the aforementioned proposed procedure in the section of "Colorimetric assay of α-glucosidase". For voglibose assay, 100 μL of voglibose with different concentrations were incubated with α-Glu.

2. Additional figures

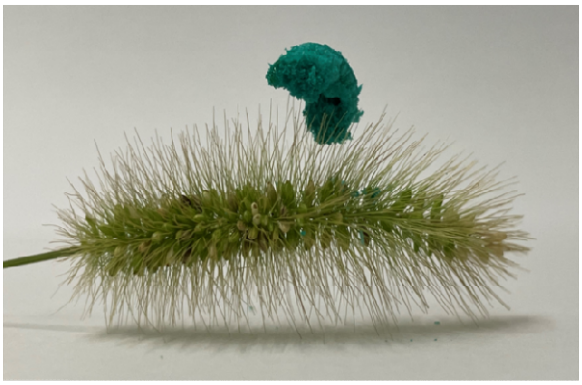

Fig. S1 Digital photographs of Cu-CD_A.

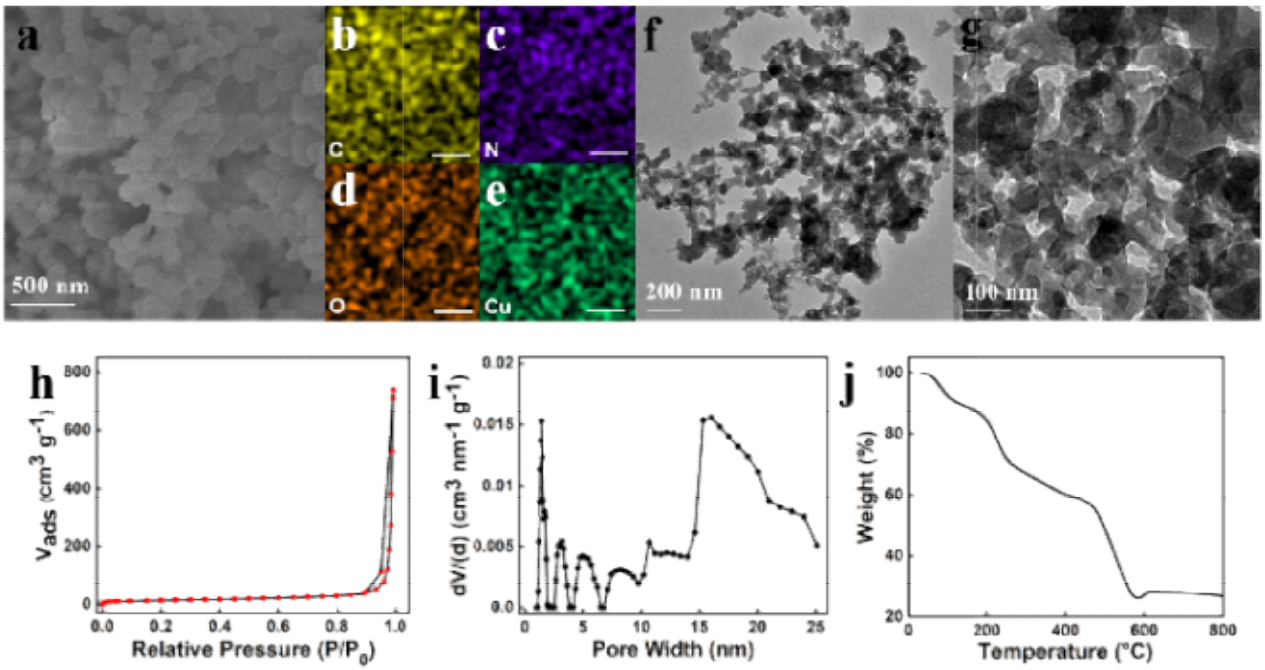

Fig. S2 (a) SEM image of Cu-CD_A, and (b-e) its corresponding element mapping images of C, N, O, and Cu, respectively. (f) TEM image of Cu-CD_A, and (g) its high-magnification TEM morphology. (h) N_2 adsorption-desorption isotherms and (i) the corresponding pore-size distributions of Cu-CD_A. (j) TGA curves of Cu-CD_A.

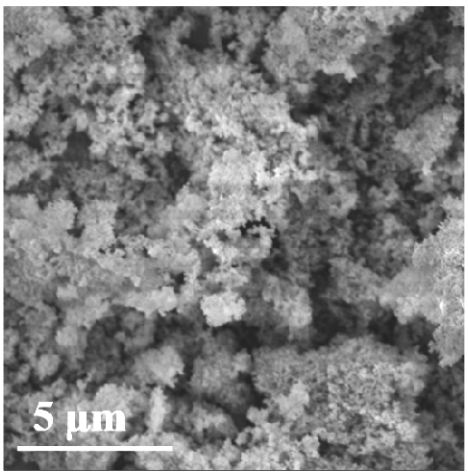

Fig. S3 SEM image of Cu-CD_A with large scan area.

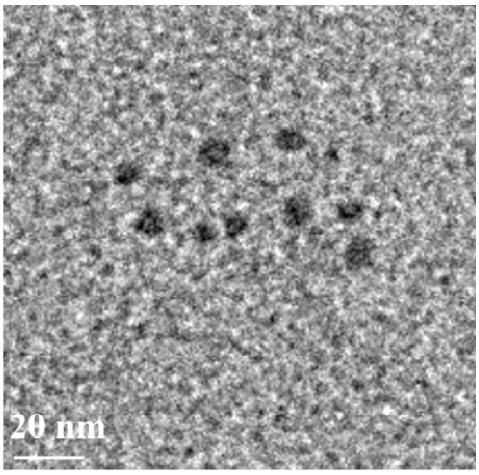

Fig. S4 TEM image of CD_A.

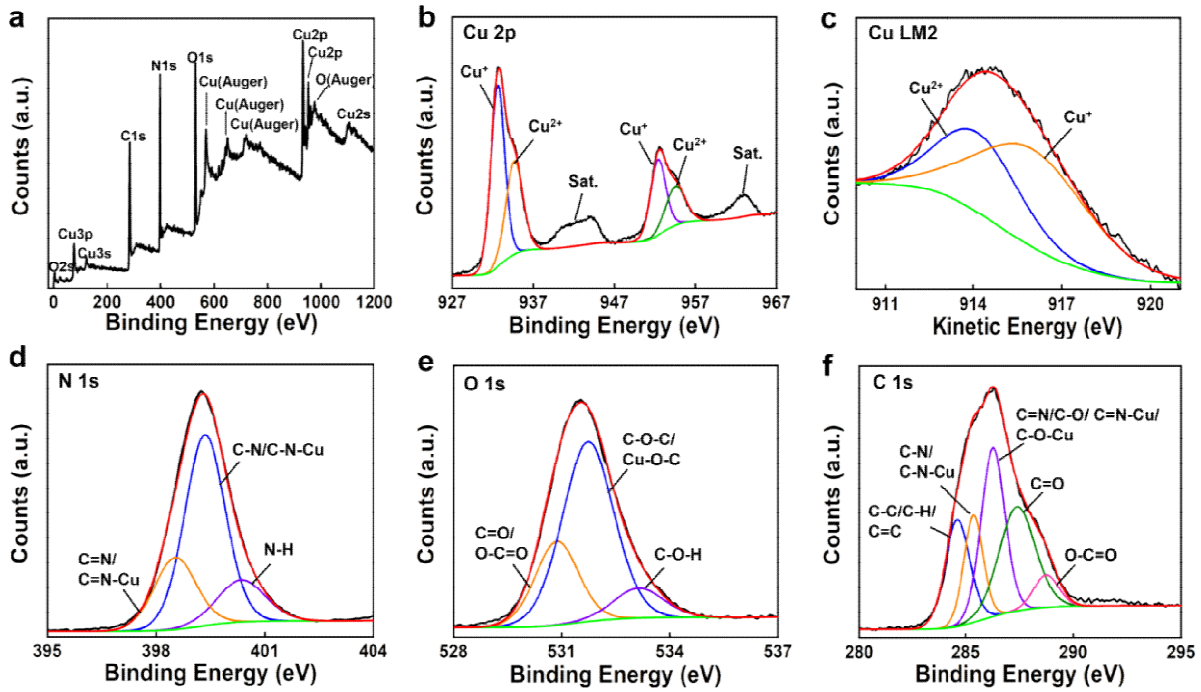

Fig. S5 (a) XPS survey spectrum, (b) Cu 2p XPS spectrum, (c) Cu LM2 Auger spectrum, (d) N 1s XPS spectrum, (e) O 1s XPS spectrum, and (f) C 1s XPS spectrum of Cu-CD_A.

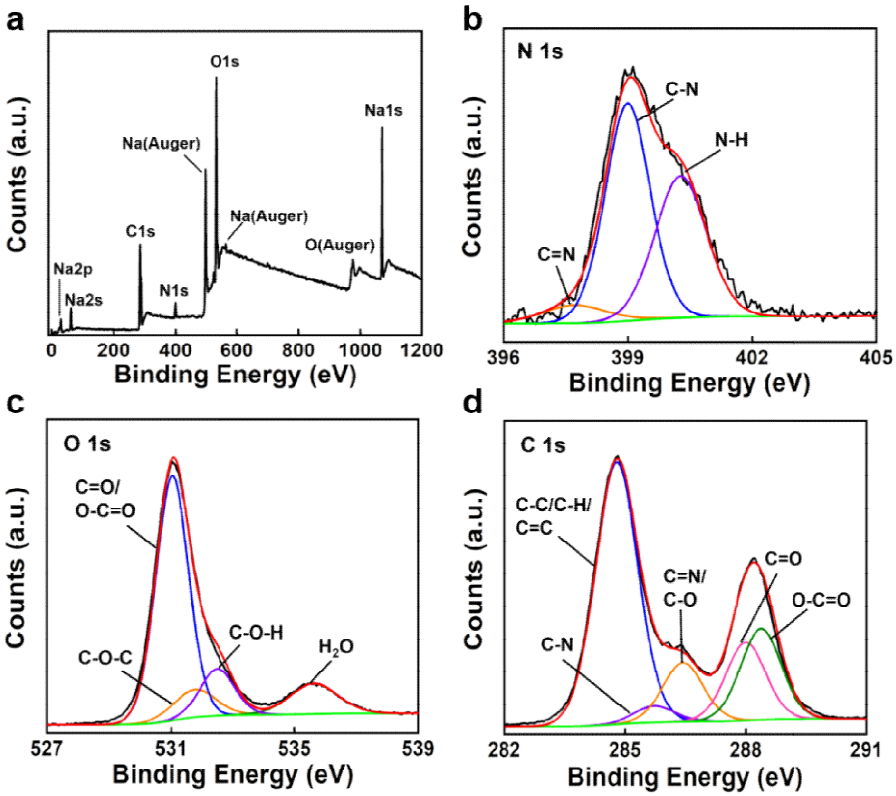

Fig. S6 (a) XPS survey spectrum of CD_A, (b) N 1s XPS spectrum, (c) O 1s XPS spectrum, and (d) C 1s XPS spectrum of CD_A.

The survey X-ray photoelectron spectroscopy (XPS) spectrum of Cu-CD_A confirms that the sample consists of Cu, N, O, and C elements (Fig. S5a), while the survey XPS spectrum of CD_A demonstrates that the CD_A contained N, O, C, and Na elements. The presence of Cu element together with the absence of Na element denotes the binding of copper ions to CD_A removes Na^+ ions (Fig. S5a and S6a). The curve-fitted Cu 2p spectrum of Cu-CD_A in Fig. S5b show that there are two intense peaks at 934.7 eV and 954.6 eV, which are assigned to Cu 2p3/2 and Cu 2p1/2 of Cu(II) species, respectively. [S1,S2] The weak shake-up satellite peaks at 940.5 eV, 943.8 eV, and 962.5 eV are clearly observed, further confirming the existence of Cu(II) species in Cu-CD_A.[S1] The other two strong peaks are located at 932.6 eV and 952.4 eV, ascribing to Cu 2p3/2 and Cu 2p1/2 of Cu(I) or Cu(0) species, respectively.[S1] Auger Cu LM2 spectrum was further used to distinguish from Cu(I) or Cu(0) species. The Auger spectrum of Cu LM2 for Cu-CD_A is divided into two peaks with the kinetic energy at 916.0 eV and 914.1 eV (Fig. S5c), which respectively correspond to the LM2 Auger lines of Cu(I) and Cu(II) species.[S1] All the results corroborate that both Cu(I) and Cu(II) species are present in the Cu-CD_A, and the Cu(II) precursor is partly reduced by the CD_A to Cu(I). Fig. S5d displays that the high resolution scan of the N 1s region in Cu-CD_A is adequately deconvoluted into three individual peaks, with binding energies at 398.5 eV, 399.4 eV, and 400.3 eV, representing C=N/C=N-Cu (23.6%), C-N/C-N-Cu (60.6%), and N-H (15.8%), respectively.[S1] The XPS spectrum of N 1s in CD_A is fitted by three components at 397.8 eV, 399.0 eV, and 400.3 eV, respectively (Fig. S6b). The three components are respectively attributed to C=N (6.4%), C-N (53.5%), and N-H (40.1%). All the N 1s XPS results demonstrate that CD_A with plentiful nitrogen-rich functional groups bind with Cu(I) and Cu(II) on the basis of Cu-N coordination chemistry. The O 1s peak in Cu-CD_A is divided into three peaks at 530.9 eV, 531.7 eV, and 533.1 eV (Fig. S5e) which are respectively attributed to C=O/O-C=O (25.2%), C-O-C/Cu-O-C (64.5%), and C-O-H (10.3%).[S1] The XPS spectrum of O 1s in CD_A shows that O is present in four different chemical environments, corresponding to C=O/O-C=O (64.5%) at 531.0 eV, C-O-C (9.7%) at 531.8 eV , C-O-H (12.3%) at 532.5 eV, and H_2O (13.5%) at 535.6 eV (Fig. S6c).[S1] All the O 1s XPS results confirm that CD_A with rich carboxyl groups are linked to the Cu species through Cu-O coordination chemistry. The high-resolution spectrum of C 1s in Cu-CD_A is fitted by five contributions at 284.6 eV, 285.4 eV, 286.3 eV, 287.4 eV, and 288.7 eV, respectively (Fig. S5f). The five contributions respectively arise from C-C/C=C/C-H, C-N/C-N-Cu, C=N/C-O/C=N-Cu/C-O-Cu, C=O, and O-C=O.[S1] Relative to CD_A, the contributions at 285.4 eV and 286.3 eV account for a comparatively high proportion of total C (Fig. S5f and Fig. S6d), further denoting that Cu species take part in the coordination interaction in the aerogels.

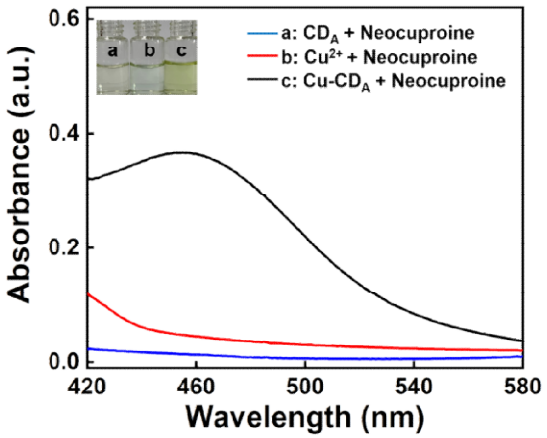

Fig. S7 UV-Vis absorption spectra of different reaction systems. Inset: the photographs of the related solution.

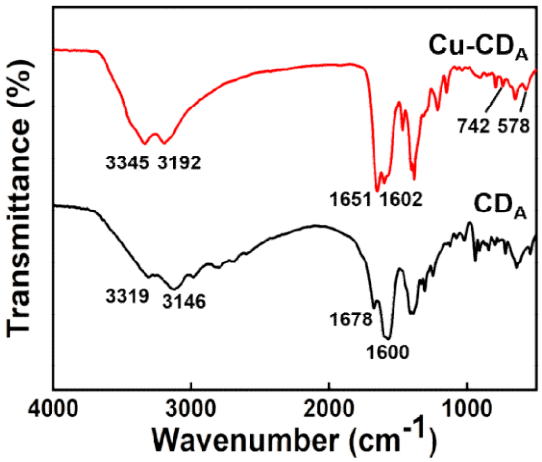

Fig. S8 FT-IR spectrum of Cu-CD_A.

FT-IR was used to reveal the surface functional groups of Cu-CD_A and CD_A. As shown in Fig. S8, CD_A has two characteristic bands at 3319 cm^{-1} and 3146 cm^{-1}, which are attributed to the O-H stretch or N-H symmetric stretch, and the N-H asymmetric stretch, respectively.[S2a-S2c] The peak at 1678 cm^{-1} is attributed to the C=O stretching motion, and the peak at 1600 cm^{-1} is characteristics of the NH_2 bending vibration.[S2a-S2c] In addition, several IR bands in the region 1580–1100 cm^{-1} are observed for CD_A, and these bands are related to the C=N stretch, C-N stretch, C-O stretch, C=C stretch, N-H deformation, C-H deformation, and ring stretch (Fig. S8).[S2a-S2c] However, after copper ion-induced self-assembly of CD_A to form Cu-CD_A, the aforementioned IR bands undergo appreciable variations in intensity and peak position, and the two new IR bands at 742 cm^{-1} and 578 cm^{-1} appear (Fig. S8), which are respectively related to the vibrations of Cu-N and Cu-O.[S2c,S2d] All the IR results give further evidence that there is the effective interaction between copper ions and the surface carboxyl and nitrogen-rich functional groups of Cu-CD_A.

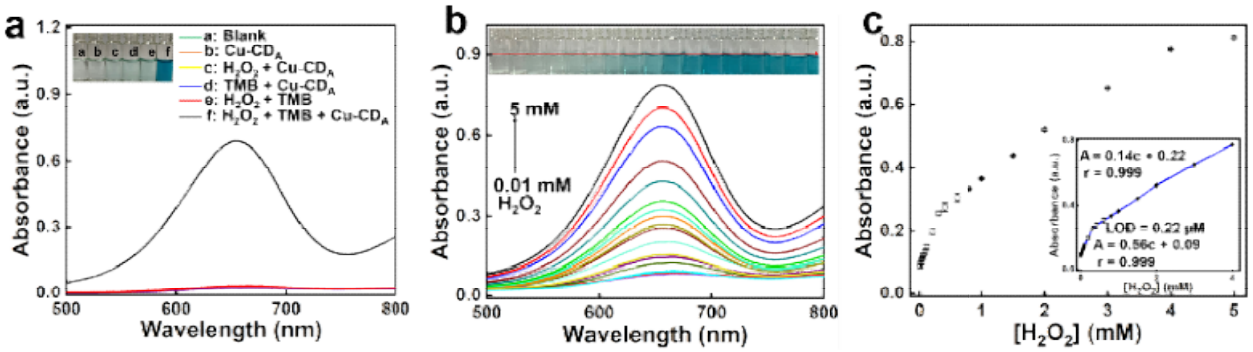

Fig. S9 (a) UV-Vis spectra of different reaction systems. Inset: the photographs of the related solution. (b) UV-Vis spectra and photographs (inset) of the oxidation of TMB catalyzed by Cu-CD_A with different concentrations of H_2O_2. (c) Plot of absorbance at 652 nm versus H_2O_2 concentration. Inset: its related linear calibration curve.

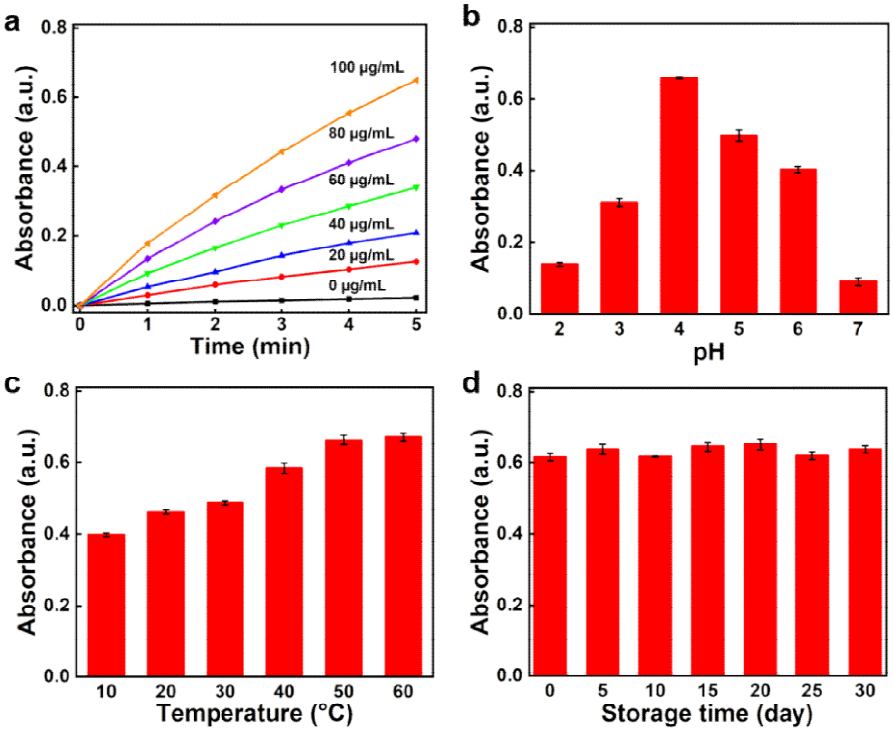

Fig. S10 (a) Time-dependent evolution of the absorbance at 652 nm for the Cu-CD_A/H_2O_2/TMB system in the presence of different concentrations of Cu-CD_A. (b) Effect of buffer pH on the absorbance at 652 nm for the Cu-CD_A/H_2O_2/TMB system. (c) Effect of temperature on the absorbance at 652 nm for the Cu-CD_A/H_2O_2/TMB system. (d) Storage stability study of the Cu-CD_A aqueous solution.

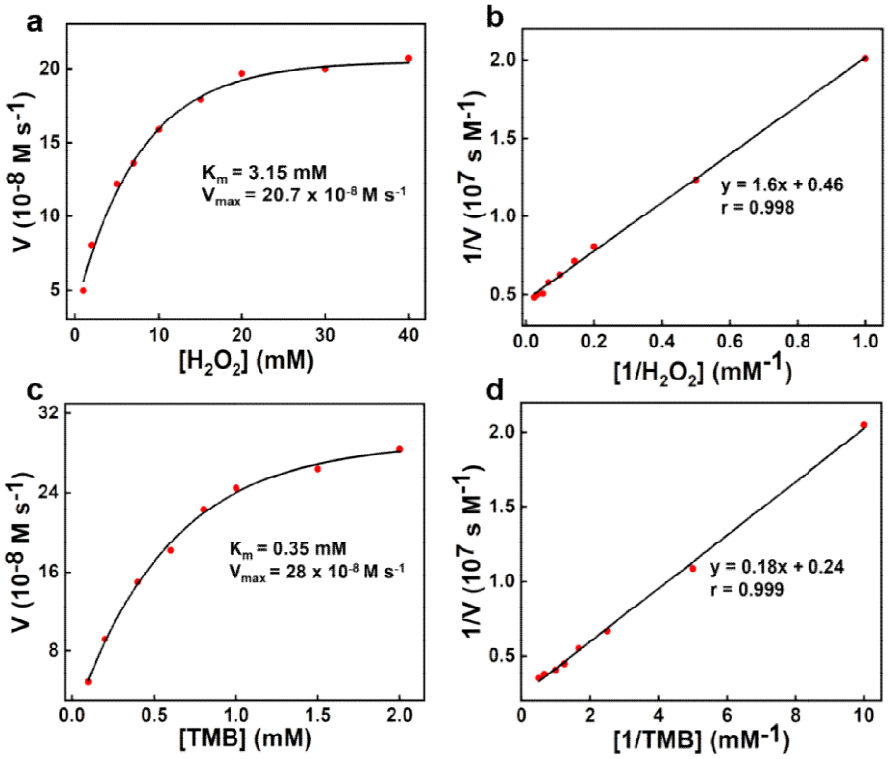

Fig. S11 Lineweaver−Burk curves of Cu-CD_A for (a) H_2O_2 and (c) TMB. Double reciprocal plots of the initial reaction rates of Cu-CD_A for (b) H_2O_2 and (d) TMB.

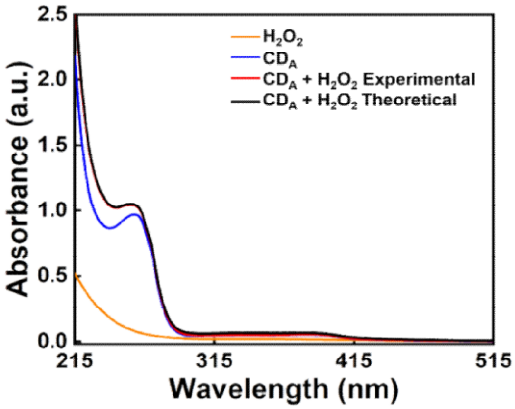

Fig. S12 UV–Vis spectra of H_2O_2 and CD_A alone, as well as the experimental and theoretical spectra based on the sum of H_2O_2 and CD_A.

Despite having the electron-accepting ability, the CD_A can hardly cause the catalytic oxidation of TMB by H_2O_2 (Fig. 1a). This is possibly because there is almost no binding of CD_A to H_2O_2, which is validated by the close resemblance between the experimental spectrum of CD_A in presence of H_2O_2 and the theoretical response of CD_A and H_2O_2 (their sum) (Fig. S12).

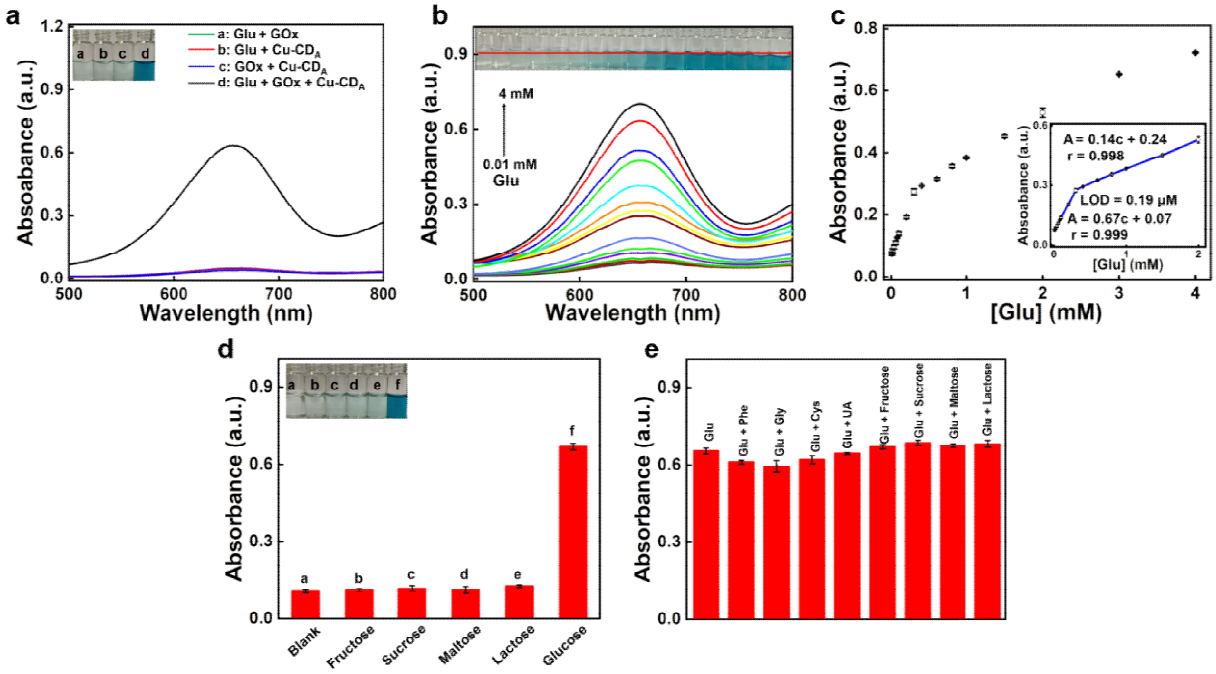

Fig. S13 (a) UV-Vis spectra of different reaction systems with TMB. Inset: the photographs of the related solution. (b) UV-Vis spectra and photographs (inset) of the GOx/Cu-CD_A cascade catalysis with different concentrations of Glu. (c) Plot of absorbance at 652 nm versus Glu concentration. Inset: its related linear calibration curve. (d) Selectivity of the GOx/Cu-CD_A-based assay for Glu over its analogues. The concentration of Glu and its analogues is 3 mM and 5 mM, respectively. (e) Interference study of the Glu assay. The concentration of Glu and other substance is 3 mM and 5 mM, respectively.

The feasibility of the Glu bioassay based on GOx/Cu-CD_A-triggered dual-enzyme cascade reactions is illustrated in Fig. S13a. Clearly, GOx alone or Glu alone can hardly trigger the Cu-CD_A-catalyzed chromogenic reaction of TMB in the absence of H_2O_2. The peroxidase-like activity of Cu-CD_A are activated in the presence of GOx and Glu, resulting in the emergence of a characteristic strong absorption band of oxTMB at 652 nm and a clear color change of TMB. Fig. S13b depicts that the absorbance at 652 nm increases gradually as Glu concentration increases. Two good linear relationships in the range of 0.01–0.3 mM (r=0.999) and 0.3–3 mM (r=0.998) are established by plotting the absorbance at 652 nm against the Glu concentration (Fig. S13c). The LOD value for Glu detection is estimated to be 0.19 μM, which is lower than or comparable well with those of most reported colorimetric Glu bioassays (Table S3). The good selectivity and anti-interference ability of the Glu bioassay can be confirmed using four typical glucose analogues (fructose, sucrose, maltose, and lactose), and the mixture containing Glu and each potential interferent (Phe, Gly, Cys, UA, fructose, sucrose, maltose, and lactose) (Fig. S13d and S13e).

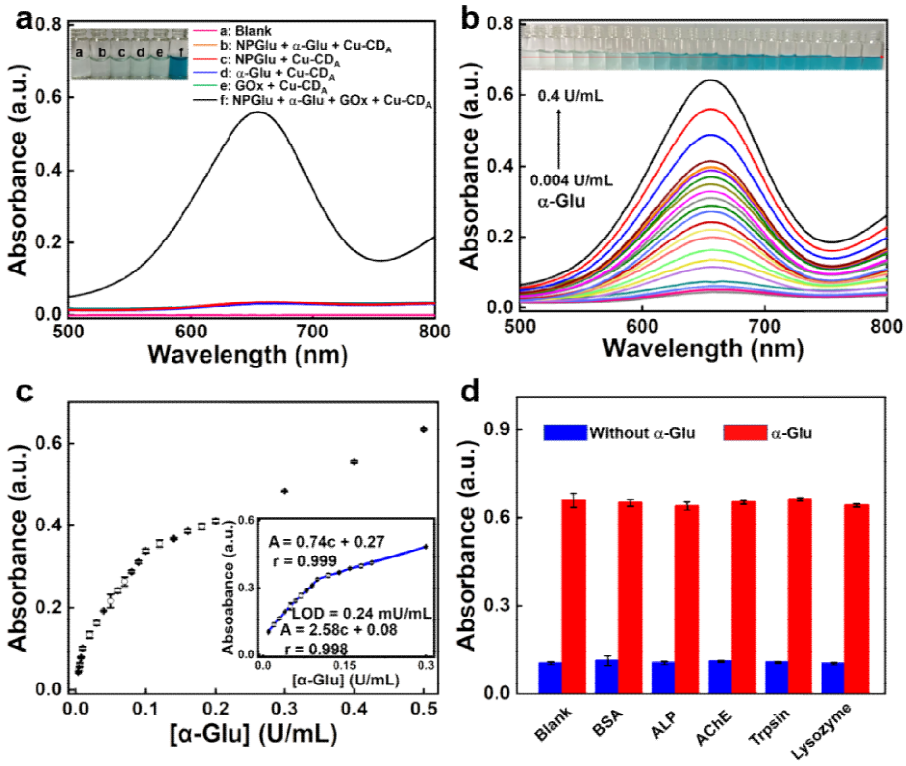

Fig. S14 (a) UV-Vis spectra of different reaction systems with TMB. Inset: the photographs of the related solution. (b) UV-Vis spectra of different reaction systems with TMB. Inset: the photographs of the related solution. (c) UV-Vis spectra and photographs (inset) of the α-Glu/GOx/Cu-CD$_A$ cascade catalysis with different activities of α-Glu. (d) Selectivity and Interference study of the α-Glu assay. The concentration of each substance is 50 μg/mL.

The bioanalysis of α-Glu activity based on α-Glu/GOx/Cu-CD$_A$-triggered triple-enzyme cascade reactions is carried out by using 4-nitrophenyl-α-D-glucopyranoside (NPGlu) as a model substrate (Fig. S14a). Obviously, only when NPGlu, α-Glu, and GOx are combined, the Cu-CD$_A$-catalyzed chromogenic reaction of TMB proceeds, demonstrating that H_2O_2 is formed through the triple-enzyme cascade reaction. As the α-Glu concentration rises, the absorbance at 652 nm increases gradually (Fig. S14b and S14c). The absorbance at 652 nm correlates linearly with the α-Glu activities in the range of 0.004−0.1 U/mL (r=0.998) and 0.1−0.3 U/mL (r=0.999), and the LOD value is estimated to be 0.24 mU/mL, which agrees well with or exceeds almost all previously reported colorimetric bioassays of α-Glu (Table S5). The good selectivity and anti-interference ability of the α-Glu bioassay can be confirmed using some proteins or enzymes such as bovine serum albumin (BSA), alkaline phosphatase (ALP), acetylcholinesterase (AChE), trypsin, and lysozyme (Fig. S14d).

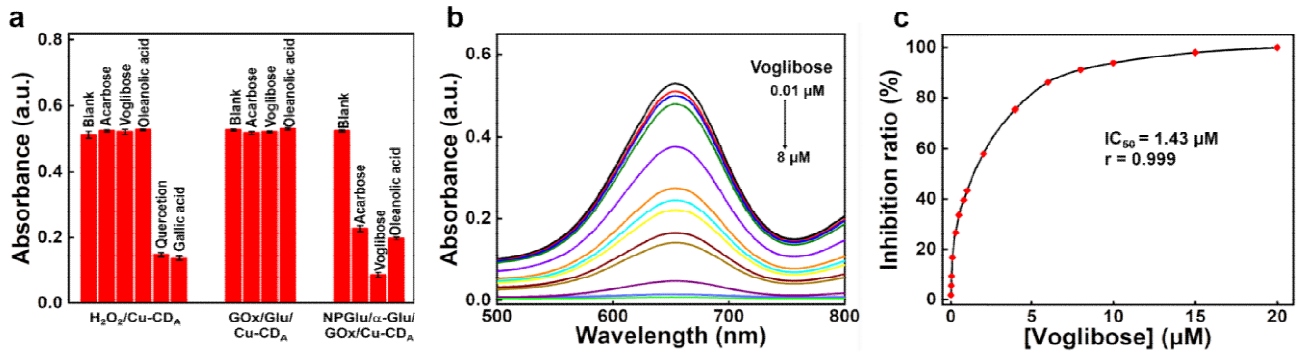

Fig. S15 (a) Influence of different AGIs on different reaction systems with TMB. (b) UV-Vis absorption spectra of the α-Glu/GOx/Cu-CD_A cascade catalysis with different concentrations of voglibose inhibitor. (c) Inhibition effect of voglibose on α-Glu activity.

The aforementioned α-Glu bioassay system is further employed to screen α-glucosidase inhibitors (AGIs) and evaluate their inhibition efficiency towards α-Glu activity for exploiting extended applications. Looking at Fig. S15a, among different AGIs, quercetin and gallic acid greatly suppress Cu-CD_A-catalyzed chromogenic reaction of TMB in the presence of H_2O_2 because of their reducing ability, while other substances, namely, acarbose, voglibose, and oleanolic acid, can only inhibit α-Glu activity but do not almost perturb the peroxidase-like activity of Cu-CD_A or GOx activity. Therefore, it is certain that the proposed triple-enzyme cascade catalysis-based approach can be used to screen AGIs with indiscernible reducing ability. Relative to acarbose and oleanolic acid, voglibose has the excellent inhibitory effect on α-Glu, and thus it is selected as the model AGI to evaluate the inhibitory efficiency towards α-Glu activity. Fig. S15b shows that the absorption band at 652 nm is gradually getting weak with the increase of voglibose concentration from 0.01 to 20 μM. The half maximal inhibitory concentration (IC_{50})is estimated to be ca. 1.43 μM (Fig. S15c). The result suggests that the proposed approach is also capable of assessing the inhibition efficiency of AGIs.

3. Additional tables

Table S1 Comparison of the performance of the Cu-CD_A aerogel-based colorimetric biosensor with other reported colorimetric biosensors for H_2O_2 detection

Material	Liner range (μM)	LOD (μM)	Reference
CD@ZIF-8[a]	100–1000	3.6	S3a
Au@Ag NR[b]	10–10000	6	S3b
Ru/PC[c]	5–1500	3.8	S3c
Ag/FeS_2[d]	20–1000	3	S3d
Fe-AL[e]	10000–100000	54	S3e
Au/Co_3O_4-CeO_x NC[f]	10–100	5.29	S3f
Fe/$CuSn(OH)_6$[g]	30–1000	9.49	S3g
Cu-CD_A aerogel	10–300	0.22	This work
	300–4000		

[a] Carbon dot@ZIF-8 framework.

[b] Gold@silver nanorod.

[c] Ruthenium nanoparticle anchored onto a porous carbon.

[d] Silver nanoparticles coupled with ferrous disulfide.

[e] Fe^{3+}-doped aminated lignin.

[f] Au/Co_3O_4-CeO_x nanocomposite.

[g] Iron doped $CuSn(OH)_6$ microsphere.

Table S2 Steady-state kinetics of Cu-CD_A, HRP, and other nanomaterials

Catalyst	TMB as substrate		H_2O_2 as substrate		Reference
	K_m (mM)	V_{max} (10^{-8} M s^{-1})	K_m (mM)	V_{max} (10^{-8} M s^{-1})	
HRP	0.43	10.0	3.7	8.71	S4a
Au hydrogel	0.32	12.3	19.92	12.8	S4b
PdCu aerogel	1.18	0.60	1.13	0.40	S4c
PdIr cube	0.13	6.5	340	5.1	S4d
Pt20	1.3	14.0	123.6	5.1	S4e
BiSA@Au-200	1.54	92.0	59.6	79.6	S4f
DPA-AuNCs aerogel	2.38	29.76	302	32.89	S4g
AuPb-NE aerogel	0.19	13.03	1.31	6.32	S4h
B, N-PdRu aerogel	2.44	5.05	0.0497	0.329	S4i
Cu-CD_A aerogel	0.35	28.0	3.15	20.7	This work

Table S3 Comparison of the performance of the GOx/Cu-CD_A-based colorimetric biosensor with other reported colorimetric biosensors for glucose detection

Material	Liner range (μM)	LOD (μM)	Reference
Ag@Fabric[a]	100–2000	80	S5a
CMS[b]	10–50	1.698	S5b
Cu-MOF@Pt[c]	2000–15000	420	S5c
CeO_2/NT-TiO_2[d]	10–500	6.1	S5d
f-FeNC[e]	10–80	0.39	S5e
	80–500		
Cu-CD_A aerogel	10–300	0.19	This work
	300-3000		

[a] Ag nanoparticle within the three-dimensional matrix of a cotton fabric.

[b] Cerium substituted $MoSe_2$ nanosheet.

[c] Cu-MOF loaded with platinum nanoparticle.

[d] Titanium dioxide nanotube with cerium dioxide.

[e] Formamide-converted iron-nitrogen-carbon.

Table S4 Determination of glucose in human serum samples

Samples	This method (mM, n = 3)	Clinical method (mM)	RSD (%, n = 3)
1	5.04±0.18	4.92	3.6
2	5.15±0.22	4.93	4.3
3	5.73±0.21	5.85	3.7

Table S5 Comparison of the performance of the α-Glu/GOx/Cu-CD_A-based colorimetric biosensor with other reported colorimetric biosensors for α-Glu detection

Material	Liner range (U/mL)	LOD (mU/mL)	Reference
NCD[a]	0.2–10	10	S6a
Si CNP[b]	0.006–3	4.6	S6b
Au-cellobiose[c]	0.003–0.1	1	S6c
pAPG-AuNP[d]	0.05–1.1	4	S6d
f-FeNC[e]	0.005–0.04	0.27	S6e
	0.04–0.1		
Cu-CD_A aerogel	0.004–0.1	0.24	This work
	0.1–0.3		

[a] Nitrogen-doped carbon dot.

[b] Silicon-containing nanoparticle.

[c] Gold-cellobiose nanocomposite.

[d] 4-aminophenyl-α-D-glucopyranoside-functionalized gold nanoparticle.

[e] Formamide-converted iron-nitrogen-carbon.

4. References

[S1] (*a*) J. F. Moulder, W. F. Stickle, P. E. Sobol and K. D. Bomben, *Handbook of X-ray Photoelectron Spectroscopy: A Reference Book of Standard Spectra for Identification and Interpretation of XPS Data.* Physcical Electronics, Minnesota, 1995; (*b*) G. Beamson and D. Briggs, *High Resolution XPS of Organic Polymers-The Scienta ESCA300 Database*, John Wiley & Sons, Chichester, 1992.

[S2] (*a*) H. H. Hammud, G. Nemer, W. Sawma, J. Touma, P. Barnabe, Y. Bou-Mouglabey, A. Ghannoum, J. El-Hajjar and J. Usta, *Chem*.*-Biol*. *Interact*., 2008, **173**, 84–96; (*b*) O. Prakash, S. K. Singh, B. Singh and R. K. Singh, *Spectrochim. Acta*, *Part A*, 2013, **112**, 410–416; (*c*) A. McNutt, S. Haq and R. Raval, *Surf. Sci*., 2003, **531**, 131–144; (*d*) N. I. Abu-Elsaad, A. S. Nawara and S. A. Mazen, *J. Phys*. *Chem*. *Solids*, 2020, **146**, 109620.

[S3] (*a*) Y. F. Wang, X. Liu, M. K. Wang, X. X. Wang, W. Y. Ma and J. Y. Li, *Sens. Actuators B Chem.*, 2021, **329**, 129115. (*b*) Y. Ding, B. Yang, H. Liu, Z. Liu, X. Zhang, X. Zheng and Q. Liu, *Sens. Actuators B Chem.*, 2018, **259**, 775–3783; (*c*) S. Y. Feng, M. Ming, M. Z. Wang, X. Wang, D. P. He, P. Jiang and Y. Y. Chen, *Chem. Commun.*, 2020, **56**, 12347–12350; (*d*) D. Li, R. Tian, S. Y. Kang, X. Q. Chu, D. H. Ge and X. J. Chen, *Food Chem.*, 2022, **393**, 133386; (*e*) L. J. Li, R. N. Zhu, B. Wang, J. Yang, F. Xu, S. Ramaswamy and X. M. Zhang, *ACS Sustainable Chem. Eng.*, 2021, **38**, 12833–12843; (*f*) H. Liu, Y. N. Ding, B. C. Yang, Z. X. Liu, Q. Y. Liu and X. Zhang, *Sens. Actuators B Chem.*, 2018, **271**, 336–345; (*g*) H. Liu, Y. N. Ding, B. C. Yang, Z. X. Liu, X. Zhang and Q. Y. Liu, *ACS Sustainable Chem. Eng.*, 2018, **6**, 14383–14393.

[S4] (*a*) L. Z. Gao, J. Zhuang, L. Nie, J. B. Zhang, Y. Zhang, N. Gu, T. H. Wang, J. Feng, D. L. Yang, S. Perrett and X. Y. Yan, *Nat*. *Nanotechnol*., 2007, **2**, 577–583; (*b*) L. Jiao, W. Q. Xu, H. Y. Yan, Y. Wu, W. L. Gu, H. Li, D. Du, Y. H. Lin and C. Z. Zhu, *Chem*. *Commun*., 2019, **55**, 9865–9868; (*c*) J. J. Huang, L. Jiao, W. Q. Xu, Q. Fang, H. J. Wang, X. L. Cai, H. Y. Yan, W. L. Gu and C. Z. Zhu, *ACS Appl*. *Mater*. *Interfaces*, 2021, **13**, 33383−33391; (*d*) X. H. Xia, J. T. Zhang, N. Lu, M. J. Kim, K. Ghale, Y. Xu, E. Mckenzie, J. Liu and H. H. Ye, *ACS Nano*, 2015, **9**, 9994−10004; (*e*) M. Moglianetti, E. De Luca, D. Pedone, R. Marotta, T. Catelani, B. Sartori, H. Amenitsch, S. F. Retta and P. P. Pompa, *Nanoscale*, 2016, **8**, 3739−3752; (*f*) H. Y. Yan, L. Jiao, H. J. Wang, Y. M. Zhu, Y. F. Chen, L. Shuai, M. Gu, M. Qiu, W. L. Gu, C. Z. Zhu, *Sens. Actuators B Chem.*, 2021, **343**, 130108; (*g*) J. Xu, F. Y. Sun, Q. Li, H. X. Yuan, F. Y. Ma, D. Wen, L. Shang, *Small*, 2022, **18**, 2200525; (*h*) R. X. Xu, X. F. Tan, T. Li, S. Q. Liu, Y. Li, H. Li, *Microchim*. *Acta*, 2021, **188**, 362; (*i*) Y. T. Zeng, Y. Li, X.

F. Tan, J. D. Gong, Z. Y. Wang, Y. H. An, Z. Q. Wang, H. Li, *ACS Appl*. *Mater*. *Interfaces*, 2021, **13**, 36816−36823.

[S5] (*a*) M. N. Karim, S. R. Anderson, S. Singh, R. Ramanathan and V. Bansal, *Biosens. Bioelectron.*, 2018, **110**, 8−15; (*b*) G. Singh, A. Ghosh, P. Pandey, A. Kushwaha, U. K. Gaur and M. Sharma, *Mater. Lett.*, 2022, **317**, 132084; (*c*) R. L. Zhou, X. H. Zhuang, Q. L. Wu, M. Jin, C. C. Zheng, Y. Y. Jiang, Y. L. Lou and L. B. Zheng, *Colloids Surf*., *B*, 2022, **216**, 112601; (*d*) H. Zhao, Y. M. Dong, P. P. Jiang, G. L. Wang and J. J. Zhang, *ACS Appl. Mater. Interfaces*, 2015, **7**, 6451−6461; (*e*) C. H. Zhang, C. X. Chen, D. Zhao, G. Kang, F. N. Liu, F. Yang, Y. Z. Lu and J. Sun, *Anal*. *Chem*., 2022, **94**, 3485−3493.

[S6] (*a*) W. Kong, D. Wu, L. Xia, X. Chen, G. Li, N. Qiu, G. Chen, Z. Sun, J. You and Y. Wu, *Anal. Chim. Acta*, 2017, **973**, 91–99; (*b*) S. Nsanzamahoro, W. F. Wang, Y. Zhang, C. B. Wang, Y. P. Shi and J. L. Yang, *Anal. Chem.*, 2021, **93**, 15412–15419; (*c*) C. Lai, G. M. Zeng, D. L. Huang, M. H. Zhao, M. Chen, Z. Wei, C. Huang, P. Xu, N. J. Li, X. Li and C. Zhang, *Anal. Methods*, 2014, **6**, 312–315; (*d*) J. Zhang, Y. Liu, J. Lv and G. Li, *Nano Res.*, 2015, **8**, 920–930; (*e*) C. H. Zhang, C. X. Chen, D. Zhao, G. Kang, F. N. Liu, F. Yang, Y. Z. Lu and J. Sun, *Anal*. *Chem*., 2022, **94**, 3485−3493.